Neurobiology of Disease

The Therapeutic Frequency Profile of Subthalamic Nucleus Deep Brain Stimulation in Rats Is Shaped by Antidromic Spike Failure

Isaac R. Cassar[1] **and Warren M. Grill**[1,2]

[1]Department of Biomedical Engineering, Duke University, Durham, North Carolina 27708 and [2]Departments of Electrical and Computer Engineering, Neurobiology, and Neurosurgery, Duke University, Durham, North Carolina 27708

The therapeutic mechanisms of subthalamic nucleus (STN) deep brain stimulation (DBS) may depend on antidromic activation of cortex via the hyperdirect pathway. However, hyperdirect pathway neurons cannot reliably follow high-stimulation frequencies, and the spike failure rate appears to correlate with symptom relief as a function of stimulation frequency. We hypothesized that antidromic spike failure contributes to the cortical desynchronization caused by DBS. We measured *in vivo* evoked cortical activity in female Sprague Dawley rats and developed a computational model of cortical activation from STN DBS. We modeled stochastic antidromic spike failure to determine how spike failure affected the desynchronization of pathophysiological oscillatory activity in cortex. We found that high-frequency STN DBS desynchronized pathologic oscillations via the masking of intrinsic spiking through a combination of spike collision, refractoriness, and synaptic depletion. Antidromic spike failure shaped the parabolic relationship between DBS frequency and cortical desynchronization, with maximum desynchronization at ~130 Hz. These findings reveal that antidromic spike failure plays a critical role in mediating the dependency of symptom relief on stimulation frequency.

Key words: **6-OHDA; antidromic spike failure; cortical evoked potential; deep brain stimulation; rat stimulation frequency**

Significance Statement

Deep brain stimulation (DBS) is a highly effective neuromodulation therapy, yet it remains uncertain why conventionally used stimulation frequencies (e.g., ~130 Hz) are optimal. In this study, we demonstrate a potential explanation for the stimulation frequency dependency of DBS through a combination of *in vivo* experimental measurements and computational modeling. We show that high-frequency stimulation can desynchronize pathologic firing patterns in populations of neurons by inducing an informational lesion. However, sporadic spike failure at these high frequencies limits the efficacy of the informational lesion, yielding a parabolic profile with optimal effects at ~130 Hz. This work provides a potential explanation for the therapeutic mechanism of DBS, and highlights the importance of considering spike failure in mechanistic models of DBS.

Introduction

Deep brain stimulation (DBS) in the subthalamic nucleus (STN) is an effective treatment for the motor symptoms of Parkinson's disease (PD) (Weaver et al., 2009; Follett et al., 2010), but the mechanism(s) of symptom relief remain uncertain (Lozano et al., 2019). The motor symptoms of PD are correlated with highly synchronous beta band oscillatory activity throughout the cortico-basal ganglia-thalamic network, and effective DBS appears to disrupt this synchronous oscillatory activity (Kuhn et al., 2008; Q. Li et al., 2012; Stein and Bar-Gad, 2013; Weiss et al., 2015; Sanders and Jaeger, 2016; Lozano et al., 2019; Johnson et al., 2020). STN DBS initiates action potentials (APs) not only in the axons of local neurons that propagate orthodromically to other basal ganglia nuclei but also in afferent axons that propagate antidromically via the hyperdirect pathway to motor cortex (M1). However, while antidromic activation of M1 alone may be sufficient to ameliorate hypokinetic symptoms in rats (Gradinaru et al., 2009; Sanders and Jaeger, 2016), it is unclear how antidromic activity contributes to desynchronization of cortical beta band activity. We conducted *in vivo* measurements of evoked cortical activity and developed a computational model of antidromic activation of cortex during STN DBS to analyze the potential effects of antidromic activity on

Received Sep. 20, 2022; revised May 22, 2023; accepted June 10, 2023.

Author contributions: I.R.C. and W.M.G. designed research; I.R.C. performed research; I.R.C. analyzed data; I.R.C. wrote the first draft of the paper; I.R.C. and W.M.G. edited the paper; I.R.C. wrote the paper.

This work was supported by National Institutes of Health Grant R37 NS040894. We thank Aaron Czeiszperger for assistance with experimental recordings; Khoa Do for conducting histology; and Danielle Degoski for laboratory support.

The authors declare no competing financial interests.

Correspondence should be addressed to Warren M. Grill at warren.grill@duke.edu.

https://doi.org/10.1523/JNEUROSCI.1798-22.2023

cortical activity. The results reveal, surprisingly, that antidromic spike failure reduces the desynchronization of cortex by STN DBS, and these findings provide a compelling explanation for the strong dependence of symptom relief on stimulation frequency that is observed clinically.

The effects of DBS on symptoms are strongly dependent on stimulation frequency, with high-frequency stimulation (HFS) between 130 and 185 Hz typically required to treat tremor and bradykinesia (Limousin et al., 1995; Moro et al., 2002; Fogelson et al., 2005), and this led to the hypothesis that DBS creates an informational lesion in the stimulated region (Grill et al., 2004). According to this theory, a combination of collision, refractoriness, and synaptic depletion during HFS masks the intrinsic activity of the stimulated neurons, thus functionally disconnecting them from the rest of the network (Grill et al., 2004). The informational lesion theory also explains why irregular stimulation is less effective (McConnell et al., 2016) and why the effects of DBS mimic those of a surgical lesion (Gross and Lozano, 2000). However, this theory does not explain the decline in therapeutic efficacy at stimulation frequencies >200 Hz (Moro et al., 2002; Q. Li et al., 2012) and assumes that the activated axons reliably follow HFS. In contrast, single-unit recordings in M1 demonstrate that hyperdirect pathway neurons activated antidromically by STN DBS are unable to follow HFS reliably for long periods of time (S. Li et al., 2007; Johnson et al., 2020). This led to an alternative theory: that sporadic failure of antidromic spikes during HFS results in asynchronous antidromic activation of cortical neurons, leading to desynchronization of pathologic oscillations and consequent reduction of symptoms (Q. Li et al., 2014).

We combined *in vivo* measurements and computational modeling to quantify the consequences of spike failure and test the hypothesis that sporadic antidromic spike failure contributes to the desynchronization of cortex during STN DBS. Surprisingly, antidromic spike failure reduced the desynchronization of beta band activity by DBS, and the greatest desynchronization occurred in scenarios with no spike failure. When spike failure was accounted for, the model predicted peak cortical desynchronization at ~130 Hz, and desynchronization declined at higher frequencies because of high rates of spike failure, closely matching the established range of DBS therapeutic efficacy (Limousin et al., 1995; Q. Li et al., 2012; Johnson et al., 2020). These results indicate that spike failure plays an important role in shaping the frequency profile of cortical desynchronization during DBS.

Materials and Methods

We developed a computational model of the antidromic effects of DBS on cortical neural activity, and validated the model with *in vivo* experimental data from the 6-hydroxydopamine (6-OHDA) hemi-lesioned rat (Betarbet et al., 2002; Deumens et al., 2002), which exhibits changes in symptoms because of regular (Limousin et al., 1995; McConnell et al., 2012) and nonregular temporal patterns of DBS (Brocker et al., 2017) similar to those observed in humans with PD. Nine female Sprague Dawley rats (250-300 g) were implanted unilaterally with stimulating microelectrodes in the STN and a bone screw above the motor cortex for electrocorticography (ECoG). The rats were rendered hemi-parkinsonian via unilateral infusion of 6-OHDA into the medial forebrain bundle. The ECoG was recorded during an awake, freely moving state while different stimulation parameters were applied, and these data were used to quantify cortical activation for model tuning and validation.

Electrode implantation and 6-OHDA lesioning

All animal care and experimental procedures were approved by the Duke University Institutional Animal Care and Use Committee. When not performing experiments, animals were housed under USDA- and Association for Assessment and Accreditation of Laboratory Animal Care-compliant conditions, with free access to food and water with a 12 h/12 h light/dark cycle. Rats were single-housed after implantation but provided extra environmental enrichment. We conducted stereotactic surgery under 3.0%-3.5% sevoflurane anesthesia using aseptic technique and coordinates from a rat brain atlas (Paxinos and Watson, 2007). Heart rate, oxygen saturation, and body temperature were monitored throughout the surgery, and the body temperature was maintained between ~35°C and 37°C with a heated water blanket. For analgesia, meloxicam (2 mg/kg s.c.) and bupivacaine (<2 mg/kg) were administered ~15 min before incision. To prevent infection, baytril (5-10 mg/kg s.c.) was administered both before incision and 24 h after, and antibiotic ointment was applied to the incision site after implantation. The cannula and electrode were implanted unilaterally and ipsilateral to each other, with the hemisphere randomized between the rats. Implantations were performed using a stereotaxic electrode manipulator and inserted manually at a rate of ~100 μm/s. One stimulating microelectrode array (2 × 2, platinum-iridium, 75 μm diameter, 0.3 mm interelectrode spacing, and 10 kΩ impedance; Microprobes) was implanted in the STN [3.6 mm posterior (P), 2.6 mm ML from bregma; 6.6-6.9 mm DV from surface of brain]. A cannula (23 gauge stainless-steel needle, cut to 1.9 cm length) was placed in the medial forebrain bundle [2.0 mm P, 2.0 mm ML from bregma; 8.5 mm from surface of skull]. In addition, stainless-steel bone screws (Fine Science Tools) were used to secure the headcap, with one bone screw located above M1 [2.5 mm anterior, 2.5 mm ML from bregma] used to record the M1 ECoG. A bone screw located above the cerebellum was used as a reference for voltage recordings. Rats were given an additional dose of meloxicam 24 h after the first dose and were monitored closely.

At 1 week after implantation, rats were lesioned under 3.0%-3.5% sevoflurane anesthesia to cause unilateral degeneration of dopaminergic neurons in the substantia nigra pars compacta (SNc). Sixty minutes before lesioning, the rats were pretreated with 50 mg/kg pargyline and 5 mg/kg desipramine injected intraperitoneally (i.p.). The 6-OHDA solution (Sigma-Aldrich; 5 mg 6-OHDA/3 ml 0.9% NaCl) was prepared immediately before use, and 10 μl was infused through the cannula at a rate of 1 μl/min. Rats were left to recover at least 1 week before any additional measurements. Lesions were assessed via methamphetamine-induced circling (see below), and circling of at least 3 turns/min in the direction ipsilateral to the lesion indicates >90% loss of dopaminergic neurons in the SNc (Ungerstedt and Arbuthnott, 1970; So et al., 2012). If this criterion was not met, rats were lesioned again, up to a total of 3 times, and secondary administrations were required in most rats.

There were two primary exclusion criteria for the implanted rats, decided *a priori*. The first was whether the rats were not adequately lesioned after three separate 6-OHDA administrations. The second was whether the stimulation electrodes were improperly placed. Improper placement was determined whether either the contact testing revealed no effective stimulation contacts or whether the postmortem histology revealed the electrode tips were outside the STN. Of the 9 rats, 4 were successful and used in this study and 2 were excluded because of improper electrode placement. Additionally, 3 were excluded because of reaching humane endpoints that required euthanasia (2 rats had skin lesions and 1 exhibited seizures following the 6-OHDA lesion).

Experimental characterization of the cortical response to STN DBS

Simultaneous STN stimulation and ECoG recording were performed while the rats were in an awake, freely moving state in their home cages. To characterize cortical activation during stimulation, we quantified the short-latency cortical evoked potential (cEP) following stimulation, which represents the aggregate, synchronous firing of the antidromically activated M1 projection neurons (Walker et al., 2012; Hartmann et al., 2018; Kumaravelu et al., 2018; Miocinovic et al., 2018; Awad et al., 2020; Gunalan and McIntyre, 2020; Johnson et al., 2020). We used the relative changes in cEP magnitude as a proxy for changes in antidromic spike success rate. For all experiments, the stimulation contacts and amplitude for each rat were those determined to be therapeutically effective during contact testing (see below).

In one set of experiments, we quantified the refractory period of the cEP. We performed a paired-pulse stimulation protocol using interpulse intervals (IPIs) from 0.5 to 1000 ms, with ones between the start of each pair of stimuli, and a total of 120 stimuli pairs applied over 2 min. The order of each 2 min stimulation session was randomized, and a 5 min washout period elapsed between sessions. The cEP magnitudes generated by the second pulse in each pair, normalized to the cEP magnitude at 1 Hz, were fit to a sigmoid, $y = \frac{1}{1+e^{(t50-t)*slope}}$ to determine the refractory period of the cEP. We used MATLAB's *Curve Fitting Tool* to perform the sigmoid fitting. From this dataset, we also quantified the average cEP latency at 1 Hz to determine the antidromic propagation time from the STN to the cortex. Each experiment was performed once in each animal.

In a second set of experiments, we characterized the cEP during eight different 3 min patterns of stimulation and used the cEP responses to each pattern to tune and validate the computational model. Of the eight patterns, five were constant frequencies [13, 50, 75, 130, 200 Hz] and three were nonregular temporal patterns of stimulation. Two of the three nonregular patterns had six 30 s blocks of constant frequency stimulation, with each block using a different constant stimulation frequency. The blocks for the first of these patterns had ascending frequencies [13, 75, 130 Hz], and the blocks for the second pattern had descending frequencies [130, 75, 13 Hz], with each set of frequencies repeated once. The third nonregular pattern had random IPIs between 5 and 500 ms, with each IPI repeated for 1 s. Each of the eight patterns were applied twice in each rat, with the order randomized and 5 min elapsed between stimulation patterns. The cEP magnitude evoked by each stimulation pulse was first averaged across the two trials for each pattern, after which we applied a moving window of 200 ms to reduce noise. Finally, to average across animals, we normalized the cEP magnitude in each trial to the average value of the cEP during the lowest frequency trial, 13 Hz, for each animal, and then averaged across animals. This yielded a normalized value of the cEP magnitude for every stimulation pulse during each of the eight stimulation patterns.

Electrical stimulation, recording, and analysis

Stimulation was conducted using an isolated voltage to current convertor (A-M Systems) controlled by MATLAB software. Charge balanced biphasic pulses (pulse width 90 μs/phase) were applied at set stimulation frequencies, with a dc filter (0.03 Hz) used to remove any dc offset. Bipolar stimulation was applied between two of the four electrodes. The stimulation amplitude and electrode contacts were determined for each rat before the start of experiments using a contact testing protocol that evaluated sustained motor responses during 130 Hz stimulation, including increased contralateral turning, decreased ipsilateral turning, increased activity, and a lack of motor side effects, including involuntary muscle contractions of the limbs and neck (So et al., 2012). Stimulation amplitudes typically varied between 50 and 100 μA.

During electrophysiological recordings, the ECoG signal was sampled at 100 kHz using a multichannel acquisition processor system (Plexon) with a 50× gain. The ECoG was analyzed offline using MATLAB. We averaged the cEP from 0 to 5 ms after stimulation and found the value and latency of the short-latency cEP peak by using MATLAB's *findpeaks* function (with default parameters) within the range of 1-3 ms after stimulus. We then quantified the magnitude, defined as the range in millivolts from the cEP peak to the point 5 ms after stimulus. This measure of magnitude, as opposed to simply the peak value, was more reliable as it was less affected by noise, and was also used to quantify human cEP magnitude (Levinson et al., 2021).

Histology

After the completion of experiments (2-6 months after implant), rats were deeply anesthetized with urethane (1.8 g/kg, i.p.) and perfused transcardially with 0.1 M PBS followed by 4% PFA in 0.1 M PBS. The brain was postfixed overnight in 4% PFA and then transferred to 30% sucrose. The brains were frozen in optimal cutting temperature compound and cut into 50 μm sections in either the coronal or horizontal planes using a cryostat (CM3050S, Leica Microsystems) and processed for two sets of staining: TH and cresyl violet. TH immunohistochemistry was used to verify the extent of degeneration of dopaminergic neurons in the SNc and electrode locations (McConnell et al., 2012; So et al., 2012; McConnell et al., 2016). Briefly, after three rinses in PBS, brain sections were first incubated for 10 min in 3% hydrogen peroxide. The sections were rinsed and blocked for 1 h at room temperature in blocking solution containing 10% goat serum. The sections were then incubated in anti-TH antibody (AB152; 1:1000, Vector Laboratories) overnight at 4°C in PBS with 10% goat serum and 0.25% Trion X-100. After three rinses in PBS, the sections were incubated with biotinylated goat antirabbit secondary antibody (BA-1000, 1:250, Vector Laboratories) with 10% goat serum and 0.25% Trion X-100 in PBS for 1 h at room temperature. After rinsing, the sections were incubated in a VECTASTAIN Elite ABC kit (Vector Laboratories) solution for 1 h and then visualized using DAB solution. Cresyl violet counter staining was used to help verify electrode locations that were compared with a rat brain atlas (Paxinos and Watson, 2007).

Computational model of the effects of STN DBS on cortical synchronization

We used a point process model (Fig. 1) composed of two groups of 250 hyperdirect pathway neurons that intrinsically fired synchronously in the beta band, and the model was implemented in MATLAB R2020b. APs propagated from the soma to two locations: down the main axon to the STN and, via a branch point, out to a single collateral synapse in the cortex. At the collateral synapse, we used a published model of stochastic vesicle release to quantify the postsynaptic conductance of each neuron (Rosenbaum et al., 2014). The postsynaptic conductances were summed across each group to produce the population conductance, which we used as a proxy of the local field potential (LFP). In one group, we introduced APs elicited by DBS in the STN that propagated antidromically up the main axon back to the soma and, via the collateral, to the synapse. As the DBS-evoked APs propagated antidromically they interacted with the intrinsic APs via collision and refractory periods. Antidromic APs that invaded the soma also altered the future firing of the soma (Q. Li et al., 2012). Finally, we introduced a model of stochastic failure of the antidromic APs that was tuned using our experimental data. Depending on the model version, spike failure was modeled to occur either at the STN branch point or at the soma.

Intrinsic somatic spiking. Intrinsic somatic spiking activity was modeled to match the experimental data from Q. Li et al. (2012), which quantified single-unit spiking of M1 corticofugal projection neurons antidromically activated by STN DBS in 6-OHDA-lesioned rats (Q. Li et al., 2012). In the lesioned condition without stimulation, these neurons had an average firing rate of ~2.5 Hz, exhibited synchronized bursts at ~0.25 Hz, had ~22% of spikes in these burst discharges, and displayed strong spectral power in the beta band from 20 to 30 Hz. We generated spike times in our model neurons using a Poisson distribution with an oscillating rate parameter to match these features. The rate parameter was the average of two waveforms: one for the β oscillations and one for the low-frequency bursting. The beta band oscillation was generated using a sinusoid with a randomly selected frequency drawn from a normal distribution with mean 25 and SD 1.5, and the same frequency was used for all neurons to produce strong beta band synchronicity. For this case, we used MATLAB's *normrnd* function, but unless specified otherwise, all other random numbers were drawn from a random uniform distribution using MATLAB's *rand* function. Each time the model was run, a different random beta band frequency was chosen, with the intent that the model be run multiple times to assess the effect of stimulation across the whole β range. The beta band oscillation waveform was generated used the equation $beta\_osc = \sin(2\pi * osc_{freq} * t)$, where osc_{freq} was the randomly selected beta band frequency. The low-frequency bursting oscillation was generated using a sinusoid with a frequency of 0.25 Hz, but with the phase randomly set between $\pm 0.5\pi$ for each neuron to match the experimental data that showed slightly offset bursts between neurons (Q. Li et al., 2012). We randomly determined a burstiness coefficient for each neuron and raised the burst oscillation to the power of the coefficient, thus matching the experimental data that showed varying degrees of burstiness between neurons (Q. Li et al., 2012). The burstiness coefficients for each neuron

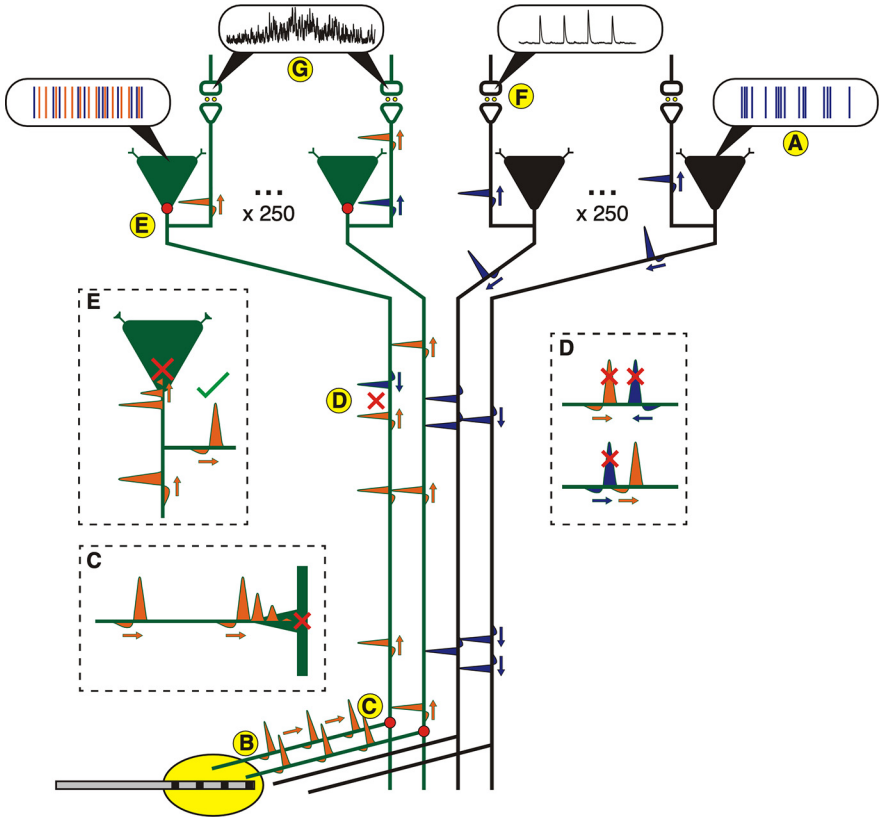

Figure 1. Model of the effects of antidromic activation of the hyperdirect pathway and spike failure on cortical neuron activity. Blue represents intrinsic APs. Orange represents antidromic APs evoked by STN DBS. Red circles represent potential locations for antidromic spike failure. Failure was modeled stochastically with a time-varying SSP that decreased after each successful AP and exponentially recovered between APs. ***A***, The 500 hyperdirect neurons were tuned to spike intrinsically with bursting behavior that was synchronized across neurons. ***B***, Half of the neurons (250) were activated by DBS in the STN collateral (green axons). These APs then propagated antidromically up the main axon to the soma and cortical collateral. ***C***, The first possible location for antidromic spike failure was at the STN branch point because of impedance mismatch. ***D***, The antidromic APs interacted with intrinsic APs via collision and refractoriness. ***E***, At the soma, antidromic APs invaded the soma to cause somatic firing, which altered the future somatic firing probabilities. The second potential location for antidromic spike failure was at the axon hillock. In this failure mode, APs successfully propagated to the cortical collateral synapse but failed to invade the soma. Only one location of antidromic spike failure was used at a time. ***F***, At the cortical collateral synapse, both antidromic and intrinsic APs caused synaptic vesicle release, which resulted in a postsynaptic conductance waveform. ***G***, The postsynaptic conductances for each neuron in each of the two groups were summed to yield population conductances, which we used as a proxy for the LFP for each group.

were drawn from a random uniform distribution between 0 and 8, which was selected to match the experimental data of the average percentage of spikes in burst discharges. The resulting burst oscillation waveform used the equation $burst\_osc = \sin(2\pi * 0.25t + rand * \frac{\pi}{2})^{rand*8}$. Burst discharges were quantified using the Poisson Surprise method (Legendy and Salcman, 1985) with a threshold of 5, which is the same method used in Q. Li et al. (2012). Finally, we averaged the two oscillations and normalized them to produce a Poisson rate parameter with the desired average firing rate, which was randomly determined for each neuron according to an exponential distribution with mean 2.5 Hz.

It is worth clarifying that, although we refer to the above firing activity of the modeled cortical neurons as intrinsic, we are not proposing that this activity was entirely self-generated. Rather, it is assumed that this firing activity is the result of various synaptic inputs. Thus, the origin or generator of the synchronous beta band activity in the cortex is not assumed to be the cortical neurons themselves, but instead may occur elsewhere in the larger motor network and propagate to the cortex.

Interactions between intrinsic activity and DBS-evoked APs. To model the interactions between DBS-evoked APs and intrinsic APs originating from the soma, we needed to know the relative refractory period of the neurons and the propagation time from the STN to the cortex. We used our experimental measurements of the cEP refractory period to generate a probability density function from which to determine randomly the refractory period for each neuron, bounded by ±0.5 ms of the mean refractory period (0.99 ± 0.5 ms). We used a two-term Gaussian distribution $y = a1 * e^{-\left(\frac{t-b1}{c1}\right)^2} + a2 * e^{-\left(\frac{t-b2}{c2}\right)^2}$, with [$a1 = 0.0043$, $b1 = 0.9913$, $c1 = 0.6077$, $a2 = 0.0029$, $b2 = 0.9846$, $c2 = 1.057$, $t = 0.49$-1.49 ms]. We used the latency of the cEP evoked by 1 Hz STN DBS to determine the propagation time, which we set to 1.31 ms (cEP latency = 1.31 ms, SEM = 0.02 ms). Using these 2 times, we modeled spike failure because of collision and refractory periods, with collision eliminating both spikes and the refractory period only eliminating the second spike.

For DBS-evoked antidromic APs that successfully invaded the soma, we modeled changes in future firing probability of each cortical neuron. In addition to the refractory period, which was accounted for above, antidromic spikes elicit both short- and long-term increases in firing probability (Q. Li et al., 2012). For each successful antidromic spike, we used a Poisson distribution to add new future somatic spikes according to the timing and firing rate determined experimentally in (Q. Li et al., 2012). The rate parameters for both time courses were fit to Gaussian distributions $\lambda = a * e^{-\left(\frac{t-b}{c}\right)^2}$, with [$a = 8.42$, $b = 2.43$, $c = 0.72$, $t = 1.6$-3.25 ms] for the short-term response and [$a = 5.28$, $b = 43.35$, $c = 8.79$, $t = 35$-51 ms] for the long-term response.

Stochastic spike failure. Prior attempts to model the mechanism of spike failure during HFS did not match experimental data (Q. Li et al., 2012; Anderson et al., 2018) and predicted findings contradictory to one another (Bellinger et al., 2008; Guo et al., 2018). We implemented a probabilistic model of stochastic spike failure designed to reproduce accurately the experimental findings, not to represent the underlying mechanism(s) of spike failure, as these are poorly understood. The model was based on a time-varying spike success probability (SSP) for each neuron that declined by a fixed amount for every successful AP and then recovered exponentially between APs. These parameters, the decrement and the recovery time constant, were tuned to match our experimental cEP data at different stimulation frequencies. However, our experimental cEP data revealed that there were three distinct time-scales for spike failure: a short-latency component that peaked between 1 and 2 s and only occurred during HFS, a medium-latency component that peaked between 30 and 60 s, and a long-latency component that peaked beyond ~300 s and caused a slow but steady decline in cEP magnitude during HFS. To match these three time-scales, we used three sets of tuning parameters, each composed of its own decrement and recovery time constant, and the resultant SSPs from each parameter set were multiplied together to yield the overall SSP. We also found in the tuning process that, for each set of tuning parameters, a third term was needed, a smaller secondary decrement that occurs after failed spikes (the primary decrement only occurred after a successful spike). Physiologically, this represents the subthreshold changes in transmembrane potential during failed spikes that still cause ion fluctuations and electrical potential changes within the neuron, albeit to a lesser degree than successful spikes.

To tune these 9 parameters, we used the model to predict the antidromic spike success rate (ASSR) at five different stimulation

frequencies [13, 50, 75, 130, 200 Hz] over time, with each stimulation frequency modeled for 180 s. Single-unit recordings indicated that at 13 Hz the ASSR is ~80% (Q. Li et al., 2012), and we normalized our experimental cEP magnitude data so the 13 Hz data had an average value of 0.8. We then quantified model fitness by comparing the ASSR to the normalized cEP magnitude data. For our cost function we quantified the average difference (AD) in experimental versus modeled spike success rate at each stimulation frequency with $AD = mean(1000*(\text{movmean}(exp - mod, 2/dt))^2)$, using MATLAB's *movmean* function. We then used particle swarm optimization to tune the parameters, implemented with MATLAB's *particleswarm* function and parallelized using the Duke Compute Cluster. We ran the particle swarm optimization 3 times using a swarm size of 100 and then took the 30 best parameter sets from each run for a final comparison. Because of the randomness in the model, we rescored these 90 patterns 25 times each, quantifying the AD as well as a second metric, the cumulative difference (CD), and selected the set of tuning parameters that had the lowest AD and CD scores. The CD metric quantified steady-state differences between the model and experimental data. First, we took the difference between the modeled and experimental success rates over time, and then then accumulated the difference across successive time points in which the difference kept the same sign, resetting the accumulation factor at every sign change. In this way, modeled success rates that made more frequent intersections with the experimental success rate scored better than those that maintained a steady-state offset. The CD was quantified with the following procedure:

v_{diff} = movmean(exp,1/dt) – movmean(mod,1/dt)
for i = 1: length(v_{diff})
  if the sign of v_{diff} changes
    $CD(1) = 0 + \text{abs}(v_{diff}(1))$
  else
    $CD(1) = CD(i\text{-}1) + \text{abs}(v_{diff}(1))$
  end
end
CD = mean(CD)

For validation, we tested the performance of the tuned model in predicting a second set of cEP experimental data obtained from the three sets of nonregular stimulation patterns [13-75-130 Hz, 130-75-13 Hz, random] and quantified performance using the AD and CD metrics. We also quantified the model's performance in predicting the changes in single-unit spiking behavior during stimulation from Q. Li et al. (2012), specifically the antidromic spike success rate, the change in somatic firing rate, and the change in somatic bursting.

Collateral synapse. Antidromic spike failure can be set to occur either at the STN branch point or at the soma. If failure occurs at the STN branch point, then the antidromic spikes do not propagate to the cortical collateral synapse, while if failure occurs at the soma, then the antidromic spikes do propagate to the cortical collateral synapse. At the collateral synapse, we modeled stochastic vesicle release using the methods from Rosenbaum et al. (2014). Each neuron was modeled with one synapse with its own store of vesicles for release. Each AP released a maximum of one vesicle, with the probability of release dependent on the number of docked vesicles ready at that time. Released vesicles then redocked over time. Each successfully released vesicle yielded a postsynaptic conductance waveform, and these were summed over the duration of stimulation. Finally, the postsynaptic conductances of each synapse were summed to yield the population conductance. We added 1/f noise to the population conductance and used the resulting signal as a proxy for the LFP, as the LFP is predominantly reflective of postsynaptic currents (Buzsáki et al., 2012). The specific parameters of the model were taken from Rosenbaum et al. (2014) [τ_1 = 4 ms, τ_2 = 1 ms, λ = 800 ms, U_w = 0.06, N_0 = 5, and J = 0.1]. We also conducted a sensitivity analysis on the parameters of the synapse model, and this showed that the primary model results were not dependent on our specific parameters.

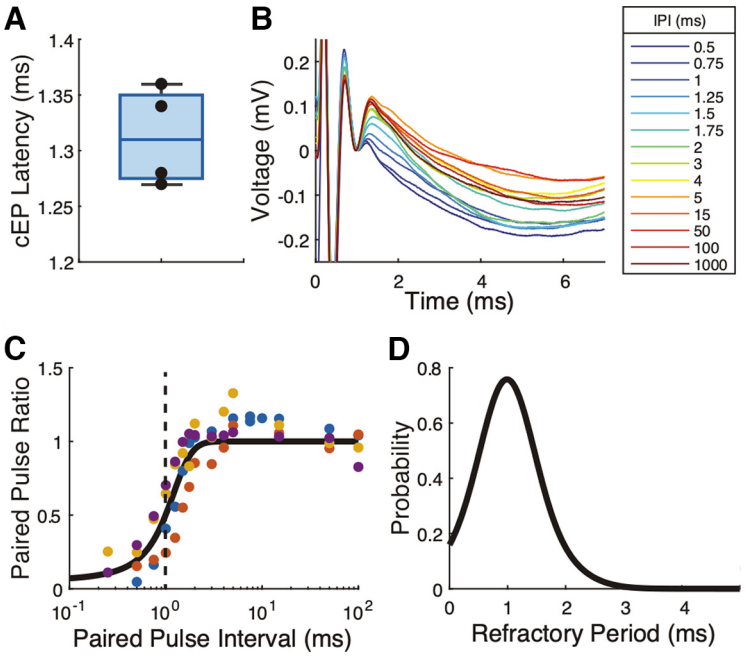

Figure 2. *In vivo* measurements of the cortical response to STN DBS in rats. Magnitude of the cEP as a function of paired-pulse interval ($n = 4$). ***A***, The average latency of the cEP evoked by 1 Hz STN DBS for each animal (mean = 1.31 ms, SEM = 0.02 ms, $n = 4$). Box plot represents the median, lower and upper quartiles, and the minimum and maximum values. ***B***, The average cEP waveform across paired-pulse intervals in a representative animal. The waveform from ~0 to 1.0 ms is the stimulation artifact. ***C***, Each cEP magnitude normalized to its value during 1 Hz stimulation. Colors represent individual values from each rat. A sigmoid was fit to the data with maximum value capped at 1 to determine the relative refractory period, which was $t_{(50)} = 0.99$ ms (dashed line). ***D***, The sigmoid from ***C*** was fit using a two-term Gaussian probability density function to determine randomly refractory periods for each model neuron.

Model outputs. Unless otherwise specified, each model was run for 120 s, and the first 30 s of each LFP (the wash-in period of stimulation) was excluded from the analysis. The primary outputs of the model were the two LFPs from the group of neurons affected by DBS and from those neurons unaffected by DBS. We were primarily interested in the beta band synchrony between these two LFP signals, as this indicates the degree to which DBS desynchronizes a target population of neurons relative to those around it. We quantified this synchronization by calculating the coherence and cross power in the beta band between the two signals using the *coherencyc* function from the Chronux MATLAB package (http://chronux.org/) (Mitra, 2007). Additionally, we were interested in how DBS affected synchronization just within the activated population, and we also quantified the synchronization metrics just within the group of neurons activated by DBS by randomly splitting the neurons in this group in two. In addition to these metrics of synchronization, we also quantified the spiking rates of the model neurons to determine the relationship between antidromic spike failure and any changes in beta band synchrony. From the antidromic spiking at the soma, we quantified the ASSR; and from the spiking at the collateral synapse, we quantified the overall rate of spikes per second, which is the ASSR multiplied by the average stimulation frequency (termed cortical activation per second [CAPS]).

Model analysis patterns. We used our model to analyze the effects of constant frequency patterns with varying stimulation frequency and random patterns with varying degrees of pattern randomness on the beta band. For each stimulation pattern, we ran the model for 120 s. For the constant frequency patterns, we applied stimulation frequencies from 0

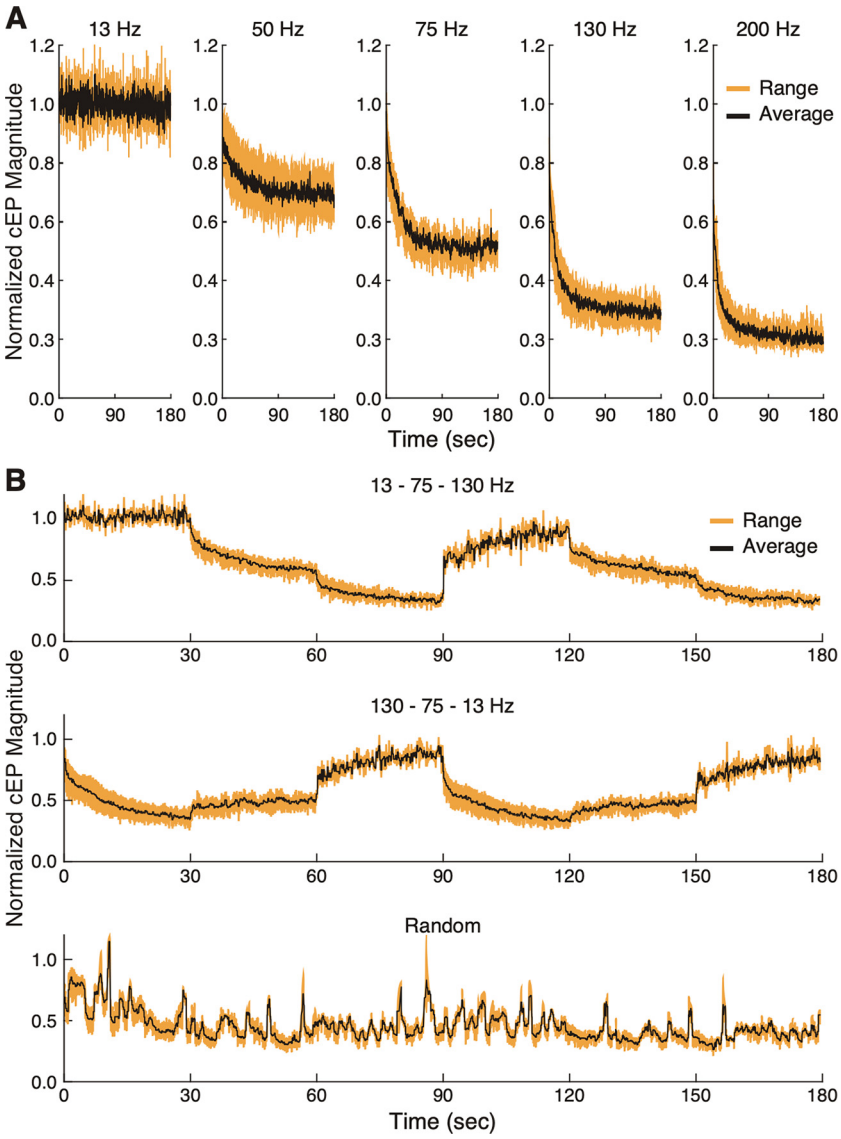

Figure 3. *In vivo* measurements of the properties of the cortical response to STN DBS in rats. Magnitude of the cEP across STN DBS rates and patterns. Each stimulation pattern was delivered for 180 s, and the cEP magnitudes for each animal ($n = 3$) were normalized to the average value for that animal during 13 Hz DBS. Black represents the average normalized cEP magnitude across animals. Yellow represents the total range of normalized cEP magnitudes across animals. ***A***, The five constant frequency patterns: 13, 50, 75, 130, and 200 Hz. ***B***, The three nonregular stimulation patterns. In the first two, six 30 s blocks of constant frequency stimulation were applied: 13, 75, 130 Hz in the top and the opposite order of 130, 75, 13 Hz in the bottom. Each group of three frequencies was repeated once. In the third nonregular pattern, we applied random IPIs varying from 5 to 500 ms (i.e., 2-200 Hz), with each IPI repeated for 1 s. The random pattern was the same for all 3 animals and resulted in a highly consistent response across animals.

to 400 Hz, with the range from 0 to 200 Hz spaced every 10 Hz and the range from 200 to 400 Hz spaced every 25 Hz. For the random patterns, we designed seven patterns to have random IPIs and an average frequency of 130 Hz. The distribution of IPIs for each pattern had increasing coefficients of variation (CV) between 0 and 4.5, testing varying degrees of pattern randomness. The patterns were generated using the methods from McConnell et al. (2016).

Experimental design and statistical analysis

We applied stimulation trains with varying patterns of IPIs to assess the average cEP responses. In one experiment ($n = 4$), we repeatedly applied 120 paired-pulses of varying IPIs, and the cEPs were averaged for each rat. These data were used to determine the refractory period and latency of the cEP. In another experiment ($n = 3$), we applied eight different 3 min patterns of stimulation, repeated twice per rat, to assess the cEP during prolonged stimulation with different IPIs. The cEP responses were averaged across trials and rats (for details, see Experimental characterization of the cortical response to STN DBS) and subsequently used for tuning the computational model. Unless otherwise stated, experimental data are presented as the mean ± SEM, and modeled data are presented as the mean ± SD. No further statistical tests were performed. We performed all data extraction from prior studies using WebPlotDigitizer version 4.4 (https://automeris.io/WebPlotDigitizer); and for some data, we quantified the z score to normalize data for plotting. The experimental cEP data used in Figures 2, 3, and 6 are available in the Duke Digital Repositories with the identifier DOI 10.7924/r41n85692.

Code accessibility

The code for the computational model used in this study is available in the Duke Digital Repositories with the identifier DOI 10.7924/r41n85692.

Results

Cortical response to STN DBS

We quantified the antidromic latency, refractory period, and the rates of antidromic spike failure from the short-latency cEP, which reflects the synchronous firing of hyperdirect neurons antidromically activated during STN DBS (Walker et al., 2012; Hartmann et al., 2018; Kumaravelu et al., 2018; Miocinovic et al., 2018; Awad et al., 2020; Gunalan and McIntyre, 2020; Johnson et al., 2020). We measured the latency of cEPs at 1 Hz to determine the propagation time (mean = 1.31, SEM = 0.02, $n = 4$, Fig. 2*A*). We quantified the refractory period using a paired-pulse paradigm with IPIs from 0.5 to 1000 ms (Fig. 2*B*). We normalized the magnitude of the cEP to the magnitude evoked at 1 Hz and fit a sigmoid $y = \frac{1}{1 + e^{(t50 - t) * slope}}$ to determine the refractory period (Fig. 2*C*), which was $t_{(50)}$ = 0.99 ms (95% CI [0.89, 1.10], $n = 4$).

In the second set of experiments ($n = 3$), we characterized the cEP using eight different patterns of DBS. The cEP amplitude declined during constant rate HFS and plateaued after ~60 s (medium-latency, Fig. 3*A*). The dynamics of the cEP also exhibited two additional phases: a near-instantaneous decline in amplitude within the first few seconds (short-latency) and a long-term decline in amplitude over multiple minutes (long-latency), both of which occurred predominantly with stimulation frequencies ≥ 130 Hz. During nonregular patterns of DBS, periods of higher-frequency stimulation resulted in smaller cEP magnitudes, and large changes in stimulation frequency were accompanied by abrupt changes in cEP magnitude of a similar time scale to the short-latency effects observed at the onset of constant frequency patterns (Fig. 3*B*). When cEP data were normalized individually to the cEP evoked at 13 Hz in each rat, there was very little variation between rats, even for the nonregular stimulation patterns, highlighting the utility of this dataset for tuning and validating the model.

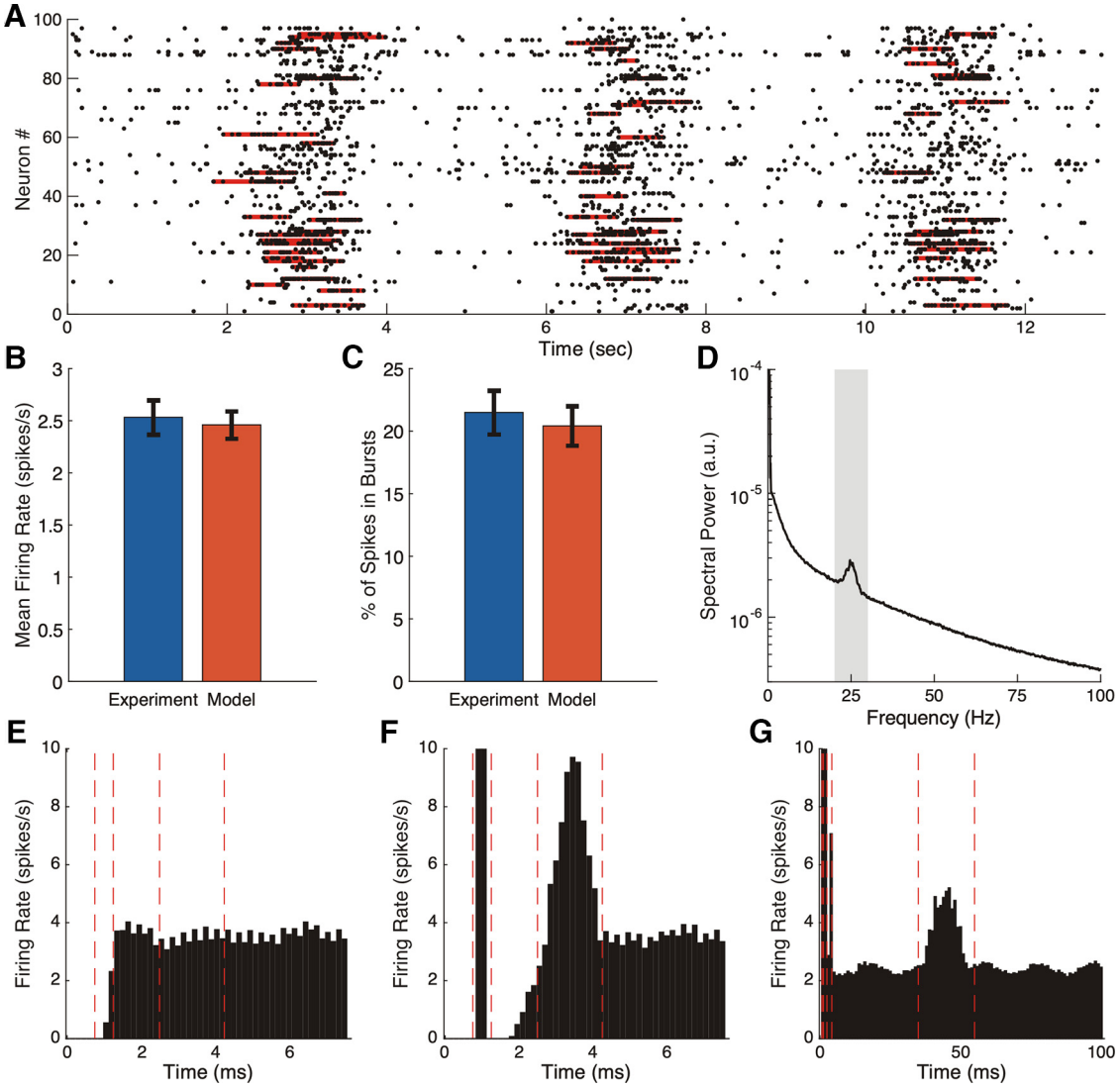

Figure 4. Characteristics of model cortical neuron activity without stimulation compared with experimental data from Q. Li et al. (2012). ***A***, Example spike raster of 100 neurons, with red lines indicating bursting periods. The synchronized bursting across neurons matched that reported in Q. Li et al. (2012). ***B***, The average firing rate of the model neurons (mean = 2.46, SD = 0.13 Hz) versus those reported experimentally in Q. Li et al. (2012) (mean = 2.53, SEM = 0.17 Hz). ***C***, The average percentage of spikes in bursts of the model neurons (mean = 20.4, SD = 1.6%) versus those reported experimentally in Q. Li et al. (2012) (mean = 21.5, SEM = 1.7%). ***D***, The average spectral power of the population conductance when averaged across 200 runs of the model. In each run, the beta oscillation frequency was randomly chosen from a normal distribution with mean 25 Hz and SD 1.5 Hz. The results closely match those seen in Q. Li et al. (2012). ***E-G***, The changes in future somatic spiking following successful antidromic invasion, which replicate the changes seen experimentally in Q. Li et al. (2012). Representative peristimulus time histograms (PSTHs) during 130 Hz stimulation, with the red lines indicating the notable time periods given in Q. Li et al. (2012). Spikes that occurred within the window around 1 ms indicated a successful antidromic spike. In Q. Li et al. (2012), time 0 was set to the time at the trough of the stimulus artifact waveform, while in our cEP recordings and model we set time 0 to the start of stimulation. Therefore, we adjusted time-zero on the *x* axis by 0.3 ms to account for that difference. ***E***, The PSTH when antidromic spikes failed to cause somatic spikes. In this case, there were no changes in spiking probability. Spiking from 0 to 1 ms was blanked to match the results from Q. Li et al. (2012), which could not record spikes in this window because of the stimulation artifact. ***F***, ***G***, The PSTH for successful antidromic spikes, which caused short-term (***F***) and long-term (***G***) increases in future somatic firing. Each somatic spike also resulted in an ~1 ms somatic refractory period (***F***).

Tuning of model parameters

We tuned parameters such that the computational model matched the single-unit spiking characteristics under basal (no-stimulation) conditions reported in Q. Li et al. (2012), and the ASSR matched our experimental cEP magnitude data during constant frequency STN DBS. For the basal case, the spiking of each neuron was modeled using a Poisson distribution with an oscillating rate parameter tuned to match the average firing rate, burstiness, and beta band power of the experimental data (Fig. 4*A*). The firing rate and burstiness were close matches (Fig. 4*B*, *C*), and the model captured the broad increase in beta band power (Fig. 4*D*). Future somatic firing probability was drawn from a Poisson distribution when an antidromic AP invaded the soma, and the neuron refractory periods were determined by randomly drawing from a two-term Gaussian probability density curve, $y = a_1 * e^{-\left(\frac{x-b_1}{c_1}\right)^2} + a_2 * e^{-\left(\frac{x-b_2}{c_2}\right)^2}$, fit from the sigmoid of the experimental refractory period data (Fig. 2*D*, $a1 = 0.004295$, $b1 = 0.9913$, $c1 = 0.6077$, $a2 = 0.002862$, $b2 = 0.9846$, $c2 = 1.057$). When antidromic spikes did not invade the soma to cause somatic spikes, there was no changes in spiking probability (Fig. 4*E*). Successful antidromic spikes generated short-term (Fig. 4*F*) and long-term (Fig. 4*G*) increases in future somatic firing probability consistent with experimental data (Q. Li et al., 2012). The short-term changes are thought to be because of changes in

intrinsic excitability caused by the antidromic AP, while the long-term changes are thought to be indicative of the delayed cortical effects of stimulation as a result of the orthodromic transmission of the AP from the STN and through the basal ganglia circuit back to cortex (Q. Li et al., 2012).

To model antidromic spike failure, we used a stochastic method composed of three different SSPs multiplied together, each tuned to represent a different time-scale [short-, medium-, and long-latency] (Fig. 5). Each of these three SSPs included three parameters: the recovery time constant, the primary decrement, and the secondary decrement, and the optimized parameter set matched the experimental data well using our AD and CD cost functions (Fig. 6*A-C*).

Validation of the model by replicating experimental data

We quantified how well the model replicated the changes in somatic spiking during STN DBS as reported in Q. Li et al. (2012), as these data were not used in the model tuning process. The model replicated the changes in somatic firing rate, percentage of spikes in burst discharges, and the ASSR at different stimulation frequencies (Fig. 7). As well, the model closely matched our experimental cEP data during the three nonregular temporal patterns of stimulation that were not used in the tuning process, with AD and CD scores equivalent to those during constant frequency stimulation (Fig. 6*D-F*).

Model-based analysis of effects of DBS and spike failure on cortical desynchronization

Our cortical model was designed with two versions, spike failure at the STN branch point or spike failure at the soma, and two potential outputs, beta band cross power and beta band coherence. To determine which combination of model version and outputs best matched experimental data, we ran each model combination with various stimulation frequencies and stimulation patterns and compared the results with experimental data (Fig. 8*A*,*B*). We first ran the models with varying stimulation frequencies from 0 to 400 Hz. There was no difference in trends between beta band cross power and coherence, but there were differences in trends for the two spike failure locations. When spike failure occurred at the STN branch point, the model predicted peak efficacy at ~130 Hz (i.e., greatest reductions in coherence and cross power). Alternatively, when spike failure occurred at the soma (i.e., all antidromic spikes propagated to the synapse), the model predicted a monotonic reduction in cross power and coherence with an asymptote at ~180 Hz. We next compared these model trends with experimental data. DBS efficacy in rats (Q. Li et al., 2012) and humans (Moro et al., 2002) improves with increasing stimulation frequency, with maximum efficacy between 130 and 185 Hz, followed by reduced efficacy at higher frequencies (Fig. 8*C*). This matches the results with spike failure at the STN branch point, but not at the soma. We also conducted a sensitivity analysis to determine whether our findings were dependent on the specific parameters used in our collateral synapse model. Importantly, the model trends of coherence and beta band cross power as a function of stimulation frequency were largely agnostic to the specific parameters of stochastic synaptic release (Fig. 9).

We also quantified the cross power and coherence as a function of the degree of randomness of the stimulation pattern. Both model versions predicted reduced coherence with increasing CV, followed by an increase in coherence with higher CV patterns (Fig. 8*D*). Conversely, both model versions predicted increased cross power with higher CVs, indicating weaker

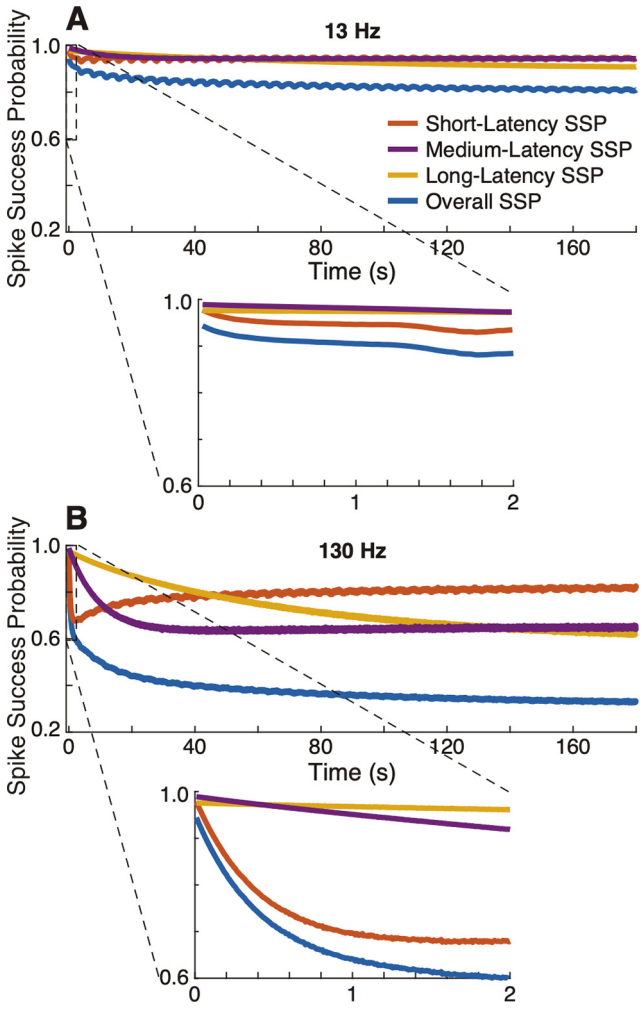

Figure 5. Example SSPs during 13 Hz (***A***) and 130 Hz (***B***) stimulation. Three sets of SSPs are quantified over time to capture the short-latency, medium-latency, and long-latency effects of stimulation. The overall SSP is the product of the three individual sets.

desynchronizing effects of high CV stimulation patterns (Fig. 8*E*). This seemingly incongruous result was because of the high CV patterns causing a strong increase in low-frequency power in the LFP. The coherence is the cross power normalized to the spectral power of each LFP, and despite the increase in beta band cross power with high CV patterns, the even larger increase in overall low-frequency power caused a decline in coherence. Stimulation patterns with highly variable IPIs are less effective than constant frequency stimulation (So et al., 2011; McConnell et al., 2016) (Fig. 8*F*), which the cross power metric accurately replicated but coherence did not.

In the above results, we quantified beta band synchronization between a group of neurons activated by DBS and a group not activated by DBS, as this is representative of the physiologically realistic scenario in which DBS activates only a subpopulation of projections to the target nucleus. We also quantified the synchronization metrics within just the group of neurons activated by DBS. The trends were largely similar to the synchronization metrics between groups, although the high CV patterns yielded much stronger coherence and cross power, even above the no-stimulation baseline, because of a broadband increase in synchronization across all frequencies. These increases in synchronization, as reflected in the coherence and cross power are consistent with the decrease in efficacy with high CV patterns

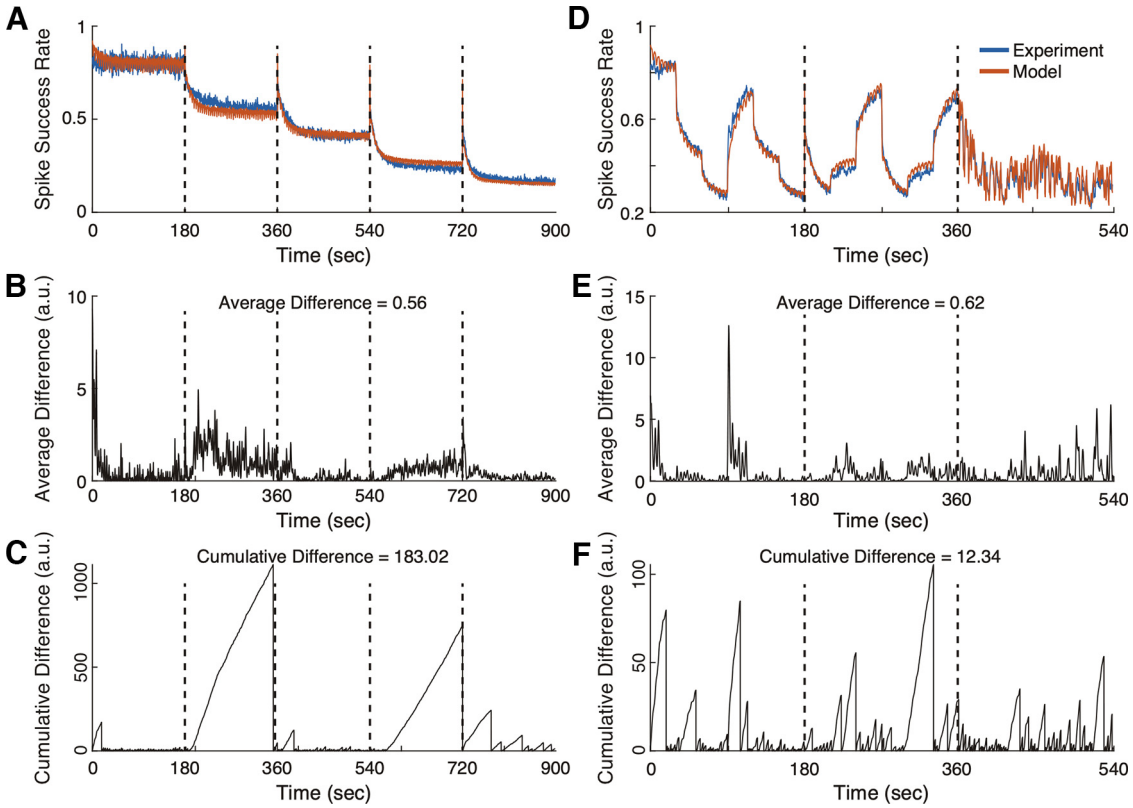

Figure 6. Comparison of model spike success rate during constant frequency stimulation (***A-C***) and nonregular stimulation (***D-F***) to experimental cEP data. Model results represent a single representative run of the model. ***A***, ***D***, Model (orange) versus experimental spike success rate (blue) over time during each stimulation pattern. The experimental spike success rate was calculated by taking the relative change in the cEP magnitude over time, normalized to an average spike success rate of 0.8 during 13 Hz stimulation. Dotted black lines indicate separate stimulation patterns that were tested independently, but the results were concatenated to quantify the difference metrics. ***B***, ***E***, The AD metric, which quantifies the average instantaneous difference between the model and experimental results. Above each plot is the average value across the whole trial. ***C***, ***F***, The CD metric, which quantifies steady-state differences between the model and experimental results. Above each plot is the average value across the whole trial. The model was just as effective at predicting the nonregular patterns in the validation dataset as it was at predicting the constant frequency patterns in the dataset used for tuning.

seen experimentally in humans (Birdno et al., 2008; Dorval et al., 2010).

We next sought to determine the relationship between antidromic spike failure and stimulation-induced desynchronization between the activated and nonactivated neurons, with the hypothesis that the antidromic spike failure rate (the inverse of the ASSR) would correlate with desynchronization. The model combination with spike failure at the branch point and beta band cross power as the output best matched the experimental data (Fig. 8). Therefore, we used the branch point spike failure model to quantify two metrics of spike failure, the ASSR and CAPS, and assessed their relationships to the beta band cross power across the same set of stimulation frequencies and stimulation patterns used previously (Fig. 10). The ASSR showed an approximately exponential decline with increasing frequency (Fig. 10*A*) and also declined as pattern CV increased (Fig. 10*B*). These patterns of antidromic spike success correlated quite poorly with the beta band cross power (r^2 = 0.003, Fig. 10*C*). In contrast, the CAPS initially increased with stimulation frequency, peaked at ~130 Hz, then declined during higher-frequency stimulation, and, as well, declined during stimulation with higher CV patterns (Fig. 10*D*,*E*). These patterns of cortical activation strongly correlated with the beta band cross power (r^2 = 0.913, Fig. 10*F*).

In contrast to our hypothesis, our model predicted that higher rates of antidromic spike failure do not contribute directly to cortical desynchronization; rather, the model predicted that the primary driver of cortical desynchronization was the overall rate of antidromic APs (the CAPS). Thus, for a given average stimulation frequency, the strongest beta band desynchronization occurred with the lowest rate of antidromic spike failure (or highest ASSR). It is worth highlighting, however, that the CAPS and ASSR are intrinsically related, as the CAPS is simply the ASSR multiplied by the stimulation frequency. Indeed, the pseudo-parabolic shape of the CAPS curve with its peak at ~130 Hz was a consequence of the shape of the exponentially decaying ASSR curve. If there was no antidromic spike failure, the ASSR would be a flat line and the CAPS would simply increase linearly with increasing stimulation frequency. Thus, the rate of antidromic spike failure as a function of stimulation frequency played a critical role in shaping the frequency profile of cortical desynchronization during STN DBS.

Discussion

We conducted *in vivo* measurements of the cortical response to STN DBS, developed a model of the effects of antidromic activation during STN DBS on cortical neuron synchronization, and demonstrated that the model replicated a broad range of published single-unit recordings and our cEP measurements. Quantifying the effects of DBS on cortical activity revealed that, in contrast to a previous hypothesis, antidromic spike failure reduced, rather than enhanced, desynchronization of cortex by STN DBS. Further, the influence of antidromic spike failure varied across stimulation

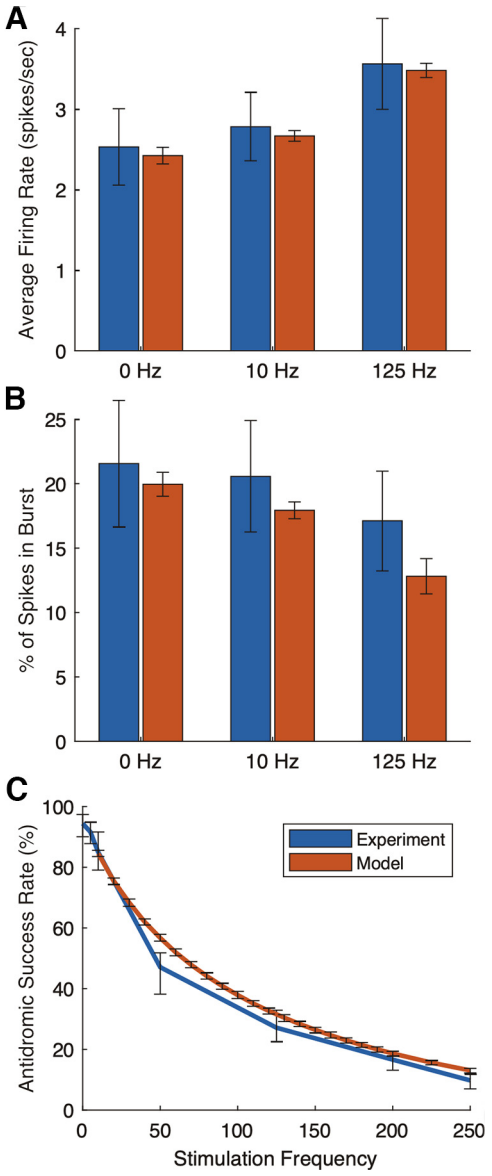

Figure 7. Characteristics of model cortical neuron activity during stimulation compared with experimental data. ***A***, The average firing rate of the model neurons at 0, 10, and 125 Hz versus those reported in Q. Li et al. (2012). The average firing rate does not include antidromic spikes. ***B***, The average percentage of spikes in bursts of the model neurons at 0, 10, and 125 Hz versus those reported in Q. Li et al. (2012). ***C***, The antidromic success rate of the model versus those reported in Q. Li et al. (2012). ***A***, ***B***, Error bars are given in SD. ***C***, Error bars represent the total range in values reported experimentally in Q. Li et al. (2012), and the range in values from 500 runs of the model at stimulation frequencies from 10 to 250 Hz.

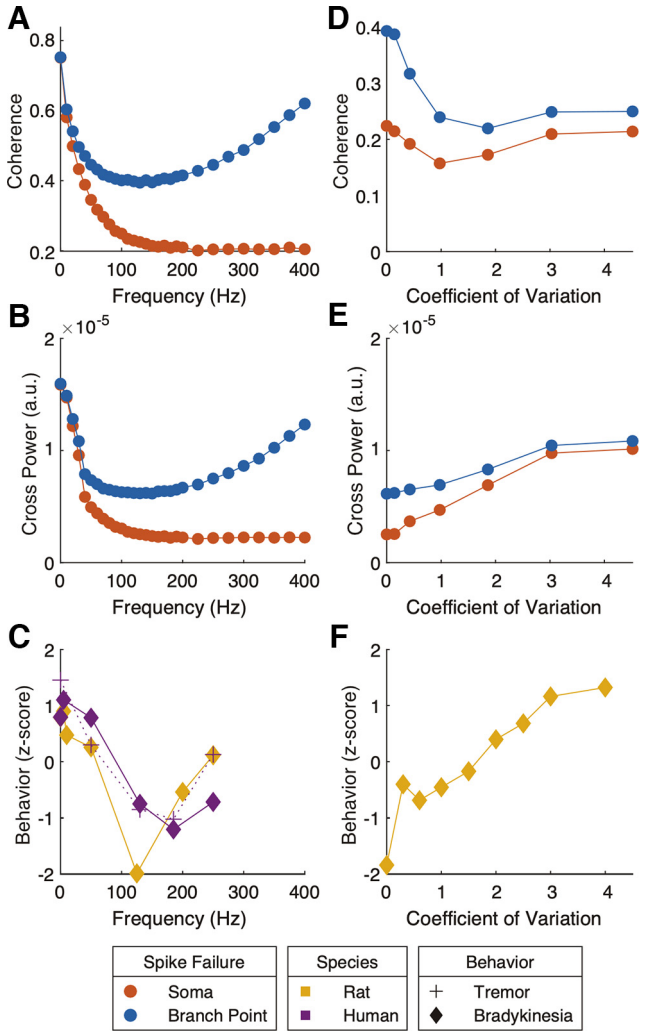

Figure 8. Beta band coherence and beta band cross power in model cortical neurons during different stimulation frequencies and patterns. (***A***) Coherence and (***B***) cross power as a function of stimulation frequency from 0 to 400 Hz. (***D***) Coherence and (***E***) cross power with random stimulation at an average stimulation frequency of 130 Hz with varying CVs of the IPIs. Colors represent the location of spike failure. Each value is the average of 500 runs of the model. ***C***, ***F***, Experimentally reported symptom reduction during DBS as a function of stimulation frequency (***C***) and CV of the IPIs (***F***), with the colors representing the species and the symbols representing the measured behavior. ***C***, The human results are taken from Moro et al. (2002), and the rat results are taken from Q. Li et al. (2012). ***F***, The results are taken from So et al. (2011).

frequencies, resulting in peak desynchronization at ~130 Hz. These findings provide a compelling explanation for the strong dependence of symptom relief on stimulation frequency.

Mechanisms of antidromic spike failure

Low-frequency STN DBS causes reliable antidromic activation of hyperdirect pathway neurons, but activation is unreliable during HFS (Q. Li et al., 2012; Johnson et al., 2020). The mechanism(s) or location(s) of antidromic spike failure are unclear. Models predict that some cortical neurons cannot maintain high rates of somatic invasion (Yi and Grill, 2018). However, antidromic spike failure in corticofugal neurons still occurred when the soma was sufficiently depolarized to guarantee somatic invasion, and failure was found most likely at the collateral branch point (Chomiak and Hu, 2007). A model that included somatic invasion failure but not failure along the axon (Anderson et al., 2018) did not match experimental antidromic spiking (Q. Li et al., 2012). These studies suggest that failure of somatic invasion alone is insufficient to account for experimentally observed antidromic spike failure.

Alternatively, there is experimental support for conduction failure along the axon. In addition to the aforementioned study showing antidromic spike failure at the branch point (Chomiak and Hu, 2007), conduction failure in the orthodromic direction during HFS has been observed elsewhere in cortex (Iremonger et al., 2006; Jensen and Durand, 2009; Feng et al., 2014, 2017) and from STN to other basal ganglia nuclei (Zheng et al., 2011; Rosenbaum et al., 2014). Because conduction failure is more likely in the antidromic than orthodromic direction (Mulloney and Selverston, 1972), likely because of impedance mismatches

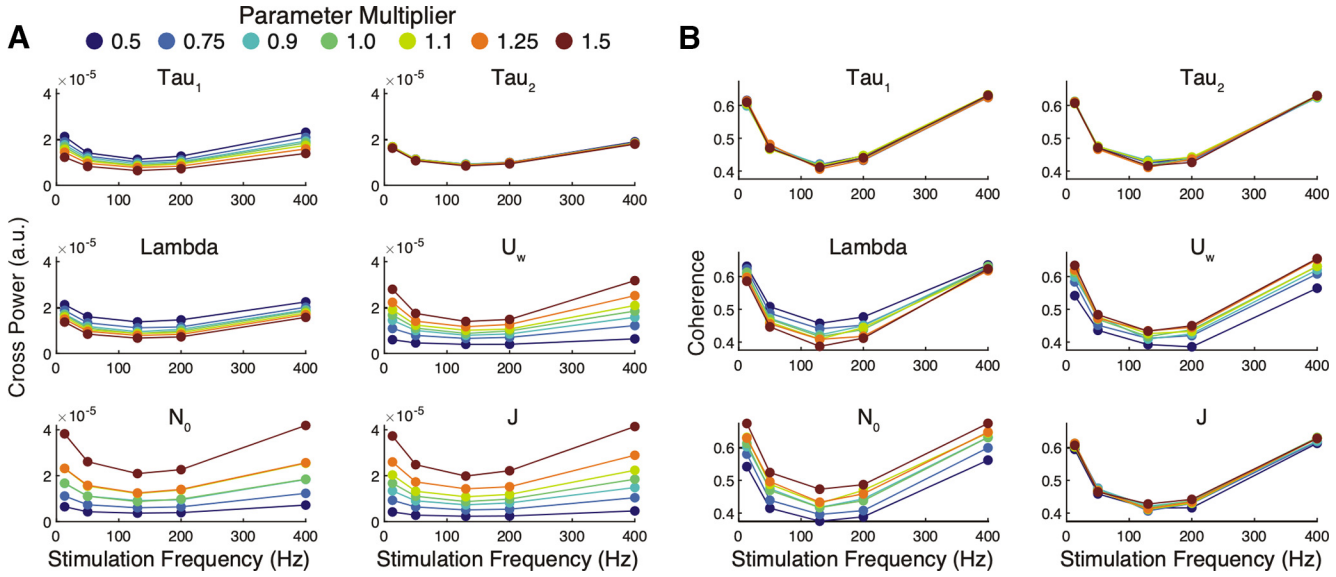

Figure 9. Sensitivity analysis of the effects of stochastic synaptic release model parameters on cross power in the beta band (***A***) and coherence in the beta band (***B***). The base value of each parameter was taken from Rosenbaum et al. (2014), and each of the six stochastic tuning parameters were individual altered by seven different multipliers [1.0 ± 0.0, 0.1, 0.25, 0.5], with the cross power and coherence quantified at five different stimulation frequencies [13, 50, 130, 200, 500 Hz]. Some parameter changes resulted in large absolute differences in cross power and coherence, but the relative differences between stimulation frequencies were unchanged.

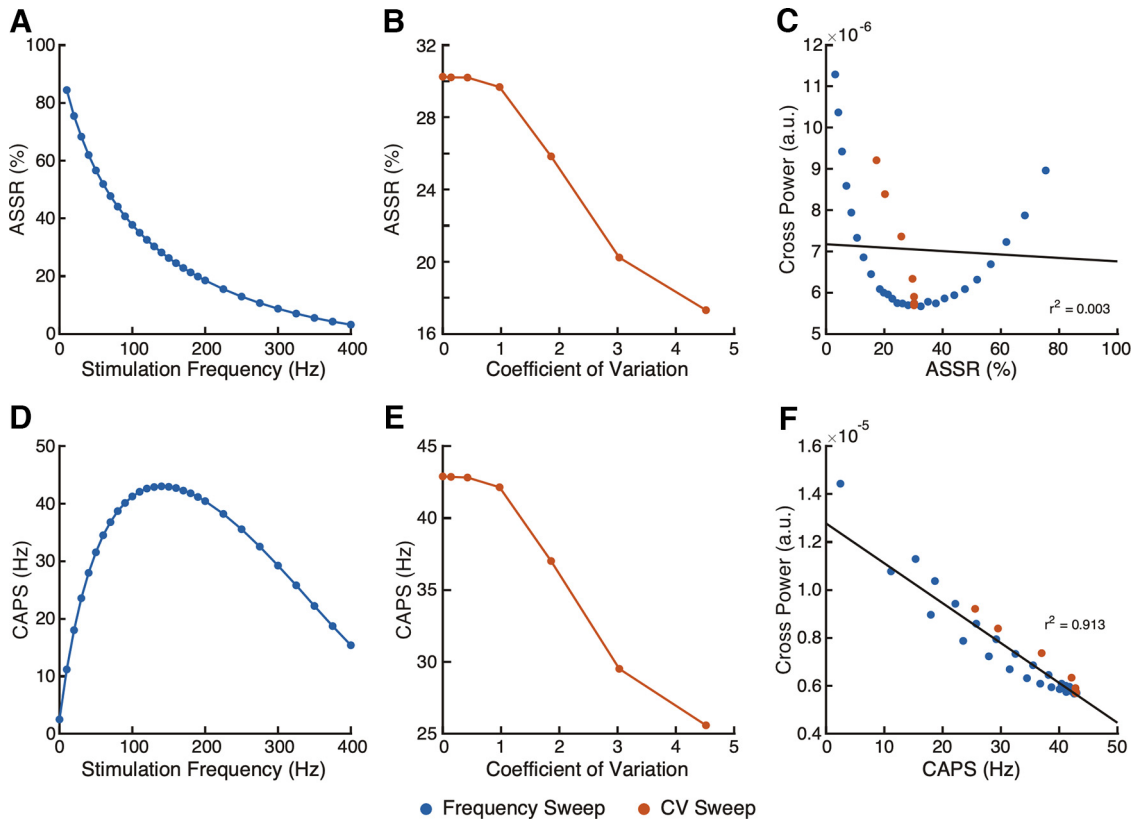

Figure 10. The relationship between antidromic spiking metrics and stimulation-induced desynchronization. Top row (***A-C***) plots the ASSR. Bottom row (***D-F***) plots the CAPS. Left column (***A***,***D***) plots each metric as a function of stimulation frequency from 0 to 400 Hz. Middle column (***B***,***E***) plots each metric during random stimulation at an average stimulation frequency of 130 Hz but varying CVs of the IPIs. Right column (***C***,***F***) plots the beta band cross power as a function of each metric, superimposing both the data across stimulation frequencies and across the CVs of IPIs (datasets represented by different colors). We also plotted the line of best fit for each combined dataset, which yielded a strong linear relationship between the CAPS and cross power ($r^2 = 0.913$), while there was no linear relationship between the ASSR and cross power ($r^2 = 0.003$).

at branch points (Grill et al., 2008), these examples of orthodromic spike failure strongly suggest that antidromic spike failure is also likely. Additionally, HFS can cause accumulation of potassium beneath the myelin that may result in conduction failure along the main axon (Bellinger et al., 2008; Brazhe et al., 2011; Guo et al., 2018). Finally, prior studies found spike failure was because of conduction block and not spike initiation failure (Robinson and Nielsen, 1990; Jensen and Durand, 2009), and thus failure to elicit a distal AP during stimulation also seems unlikely.

Our results support the location of spike failure at the STN collateral. When spike failure occurred at the soma, the model predicted sustained cortical desynchronization at stimulation frequencies >200 Hz, but when spike failure occurred at the STN branch point, maximum desynchronization occurred at ~130 Hz and declined at higher frequencies. STN DBS at stimulation frequencies >200 Hz is less effective than at 130-185 Hz in rats (Q. Li et al., 2012) and humans (Moro et al., 2002), consistent with our model results only when failure occurred at the STN branch point (Fig. 8).

Stimulation-induced desynchronization

Excessive beta band synchronization throughout the cortico-basal ganglia-thalamic network is correlated with motor symptoms in PD, and effective DBS reduces this synchrony (Kuhn et al., 2008; Q. Li et al., 2012; Stein and Bar-Gad, 2013; Weiss et al., 2015; Sanders and Jaeger, 2016; Lozano et al., 2019; Johnson et al., 2020). It is not known where the beta band oscillations are initiated, but potential sources include alterations in STN–GPe coupling (Holgado et al., 2010; Pavlides et al., 2012), long-loop resonance between the cortex and basal ganglia (West et al., 2018), and aberrant striatal–GP firing (McCarthy et al., 2011; Crompe et al., 2020). We do not propose an initiator of beta band activity, but instead assess how DBS may disrupt ongoing synchronous beta band activity within the cortex, wherever it may originate. The motor cortex is of interest because it expresses excessive beta activity that is ameliorated by DBS (Q. Li et al., 2012), and antidromic activation of cortex during STN DBS appears to play a critical role in therapeutic mechanisms (Gradinaru et al., 2009; Sanders and Jaeger, 2016; Yu et al., 2020).

In our work, we demonstrate that high-frequency STN DBS desynchronized local populations of cortical neurons without having to engage network-dependent mechanisms; this desynchronization was characterized by three main trends.

First, contrary to the hypothesis of Q. Li et al. (2014), desynchronization was not increased by antidromic spike failure but rather was approximately linearly related to the overall activation rate of the cortical collateral synapse (Fig. 10*F*). Cortical desynchronization thus resulted from masking intrinsic spiking through a combination of spike collision, refractoriness, and synaptic depletion, consistent with the informational lesion (Grill et al., 2004).

Second, although desynchronization was primarily a function of the CAPS, it also was affected by stimulation pattern regularity. Stronger desynchronization was caused by more regular stimulation patterns, as nonregular patterns with the same CAPS as constant frequency patterns generated less desynchronization (Fig. 10*F*).

Third, the CAPS is a function of average stimulation frequency and antidromic spike failure rate, and both features are critical to consider. Prior modeling of the informational lesion did not include spike failure and predicted maximal efficacy across high-stimulation frequencies (Grill et al., 2004). This is akin to our model with spike failure at the soma, which predicted the same trend. However, when we modeled a realistic location and rate of antidromic spike failure, the masking effect from the informational lesion was no longer monotonic with stimulation frequency, and desynchronization instead followed a parabolic curve with its peak at ~130 Hz (Fig. 8*A*), a pattern that matched DBS efficacy with frequency in rats (Q. Li et al., 2012) and humans (Moro et al., 2002). The shape of this parabolic relationship was because of the synaptic activation rate being the product of two approximately linear, yet opposite, relationships: the stimulation frequency and the spike failure rate. Antidromic spike failure thus does not appear to promote desynchronization, as was hypothesized, but spike failure remains critical in shaping the frequency profile of symptom reduction. These results thus support the mechanism of the informational lesion but provide a critical upper limit after which efficacy declines because of failure of antidromic DBS-evoked spikes.

Implications for orthodromic activation

These results indicate that DBS can desynchronize target populations of neurons, and this desynchronization may contribute to the therapeutic mechanism of DBS. We focused on antidromically activated cortical neurons, as optogenetic studies demonstrated sufficiency of activating projections to STN to produce therapeutic effects (Gradinaru et al., 2009; Sanders and Jaeger, 2016). Nonetheless, activation of STN orthodromic projections may also contribute to the symptom reduction, and high-frequency optogenetic activation of only the orthodromic projections from STN is sufficient to cause symptom reduction (Yu et al., 2020). However, orthodromic APs are also susceptible to conduction failure during HFS, although failure rates are challenging to assess as they must be distinguished from synaptic failure (Zheng et al., 2011; Rosenbaum et al., 2014). Our results suggest considering the effects of axonal spike failure on orthodromic mechanisms by incorporating models of spike failure (Rosenbaum et al., 2014) in network models of DBS (Kumaravelu et al., 2016, 2018; Farokhniaee and Lowery, 2021).

Scope and limitations

Our model incorporated a phenomenological representation of antidromic spike failure, as the underlying mechanisms are unclear and biophysically realistic models of hyperdirect pathway activation do not reproduce experimental levels of spike failure (Q. Li et al., 2012; Anderson et al., 2018). Importantly, the objective was not to model the mechanism of spike failure, but rather to determine the potential consequences of spike failure, and our comprehensive validation of our model provided confidence in predicting physiological rates of antidromic spike failure.

Our cEP measurements revealed three time-scales in the dynamics of antidromic spike failure, and all three occurred at the same location in the model. However, the three time-scales may relate to different mechanisms of spike failure that may occur at different locations, including at the branch point (Chomiak and Hu, 2007), along the main axon (Guo et al., 2018), or at the soma (Yi and Grill, 2018). Unfortunately, with the available experimental data, it was not possible to tune model versions accurately with spike failure occurring at multiple locations, as there were numerous model versions that all matched the same experimental data (not shown).

The model did not include potential recurrent mechanisms from the output back onto model neurons. This ensured a

conservative estimate of the desynchronizing effects of DBS, as the intrinsic spiking drove high levels of β synchronization regardless of desynchronization of the output. Given the importance that the cortico-basal ganglia feedback loop provides in propagating and maintaining beta band synchronization (West et al., 2018), presumably a reduction in β synchronization in the model outputs would reduce the recurrent drive of cortical beta band synchronization, thereby further increasing desynchronizing.

References

Anderson RW, Farokhniaee AA, Gunalan K, Howell B, McIntyre CC (2018) Action potential initiation, propagation, and cortical invasion in the hyperdirect pathway during subthalamic deep brain stimulation. Brain Stimul 11:1140–1150.

Awad MZ, Irwin ZT, Vaden RJ, Guthrie BL, Walker HC (2020) Short latency cortical evoked potentials elicited by subthalamic nucleus deep brain stimulation: commentary and results from paired-pulse studies. Clin Neurophysiol 131:465–467.

Bellinger SC, Miyazawa G, Steinmetz PN (2008) Submyelin potassium accumulation may functionally block subsets of local axons during deep brain stimulation: a modeling study. J Neural Eng 5:263–274.

Betarbet R, Sherer TB, Greenamyre JT (2002) Animal models of Parkinson's disease. BioEssays 24:308–318.

Birdno MJ, Kuncel AM, Dorval AD, Turner DA, Grill WM (2008) Tremor varies as a function of the temporal regularity of deep brain stimulation. Neuroreport 19:599–602.

Brazhe AR, Maksimov GV, Mosekilde E, Sosnovtseva OV (2011) Excitation block in a nerve fibre model owing to potassium-dependent changes in myelin resistance. Interface Focus 1:86–100.

Brocker DT, Swan BD, So RQ, Turner DA, Gross RE, Grill WM (2017) Optimized temporal pattern of brain stimulation designed by computational evolution. Sci Transl Med 9:eaah3532.

Buzsáki G, Anastassiou CA, Koch C (2012) The origin of extracellular fields and currents: EEG, ECoG, LFP and spikes. Nat Rev Neurosci 13:407–420.

Chomiak T, Hu B (2007) Axonal and somatic filtering of antidromically evoked cortical excitation by simulated deep brain stimulation in rat brain. J Physiol 579:403–412.

Crompe B, Aristieta A, Leblois A, Elsherbiny S, Boraud T, Mallet NP (2020) The globus pallidus orchestrates abnormal network dynamics in a model of Parkinsonism. Nat Commun 11:1570.

Deumens R, Blokland A, Prickaerts J (2002) Modeling Parkinson's disease in rats: an evaluation of 6-OHDA lesions of the nigrostriatal pathway. Exp Neurol 175:303–317.

Dorval AD, Kuncel AM, Birdno MJ, Turner D, Grill WM (2010) Deep brain stimulation alleviates parkinsonian bradykinesia by regularizing pallidal activity. J Neurophysiol 104:911–921.

Farokhniaee A, Lowery MM (2021) Cortical network effects of subthalamic deep brain stimulation in a thalamo-cortical microcircuit model. J Neural Eng 18:056006.

Feng Z, Yu Y, Guo Z, Cao J, Durand DM (2014) High frequency stimulation extends the refractory period and generates axonal block in the rat hippocampus. Brain Stimul 7:680–689.

Feng Z, Wang Z, Guo Z, Zhou W, Cai Z, Durand DM (2017) High frequency stimulation of afferent fibers generates asynchronous firing in the downstream neurons in hippocampus through partial block of axonal conduction. Brain Res 1661:67–78.

Fogelson N, Kühn AA, Silberstein P, Limousin PD, Hariz M, Trottenberg T, Kupsch A, Brown P (2005) Frequency dependent effects of subthalamic nucleus stimulation in Parkinson's disease. Neurosci Lett 382:5–9.

Follett KA, et al., CSP 468 Study Group (2010) Pallidal versus subthalamic deep-brain stimulation for Parkinson's disease. N Engl J Med 362:2077–2091.

Gradinaru V, Mogri M, Thompson KR, Henderson JM, Deisseroth K (2009) Optical deconstruction of parkinsonian neural circuitry. Science 324:354–359.

Grill WM, Snyder AN, Miocinovic S (2004) Deep brain stimulation creates an informational lesion of the stimulated nucleus. Neuroreport 15:1137–1140.

Grill WM, Cantrell MB, Robertson MS (2008) Antidromic propagation of action potentials in branched axons: implications for the mechanisms of action of deep brain stimulation. J Comput Neurosci 24:81–93.

Gross RE, Lozano AM (2000) Advances in neurostimulation for movement disorders. Neurol Res 22:247–258.

Gunalan K, McIntyre CC (2020) Biophysical reconstruction of the signal conduction underlying short-latency cortical evoked potentials generated by subthalamic deep brain stimulation. Clin Neurophysiol 131:542–547.

Guo Z, Feng Z, Wang Y, Wei X (2018) Simulation study of intermittent axonal block and desynchronization effect induced by high-frequency stimulation of electrical pulses. Front Neurosci 12:858.

Hartmann CJ, Hirschmann J, Vesper J, Wojtecki L, Butz M, Schnitzler A (2018) Distinct cortical responses evoked by electrical stimulation of the thalamic ventral intermediate nucleus and of the subthalamic nucleus. Neuroimage Clin 20:1246–1254.

Holgado AJ, Terry JR, Bogacz R (2010) Conditions for the generation of beta oscillations in the subthalamic nucleus–globus pallidus network. J Neurosci 30:12340–12352.

Iremonger KJ, Anderson TR, Hu B, Kiss ZH (2006) Cellular mechanisms preventing sustained activation of cortex during subcortical high-frequency stimulation. J Neurophysiol 96:613–621.

Jensen AL, Durand DM (2009) High frequency stimulation can block axonal conduction. Exp Neurol 220:57–70.

Johnson LA, Wang J, Nebeck SD, Zhang J, Johnson MD, Vitek JL (2020) Direct activation of primary motor cortex during subthalamic but not pallidal deep brain stimulation. J Neurosci 40:2166–2177.

Kuhn AA, Kempf F, Brucke C, Gaynor Doyle L, Martinez-Torres I, Pogosyan A, Trottenberg T, Kupsch A, Schneider GH, Hariz MI, Vandenberghe W, Nuttin B, Brown P (2008) High-frequency stimulation of the subthalamic nucleus suppresses oscillatory activity in patients with Parkinson's disease in parallel with improvement in motor performance. J Neurosci 28:6165–6173.

Kumaravelu K, Brocker DT, Grill WM (2016) A biophysical model of the cortex-basal ganglia-thalamus network in the 6-OHDA-lesioned rat model of Parkinson's disease. J Comput Neurosci 40:207–229.

Kumaravelu K, Oza CS, Behrend CE, Grill WM (2018) Model-based deconstruction of cortical evoked potentials generated by subthalamic nucleus deep brain stimulation. J Neurophysiol 120:662–680.

Legendy C, Salcman M (1985) Bursts and recurrences of bursts in the spike trains of spontaneously active striate cortex neurons. J Neurophysiol 53:926–939.

Levinson LH, Caldwell DJ, Cronin JA, Houston B, Perlmutter SI, Weaver KE, Herron JA, Ojemann JG, Ko AL (2021) Intraoperative characterization of subthalamic nucleus-to-cortex evoked potentials in Parkinson's disease deep brain stimulation. Front Hum Neurosci 15:590251.

Li Q, Ke Y, Chan DC, Qian ZM, Yung KK, Ko H, Arbuthnott GW, Yung WH (2012) Therapeutic deep brain stimulation in parkinsonian rats directly influences motor cortex. Neuron 76:1030–1041.

Li Q, Qian ZM, Arbuthnott GW, Ke Y, Yung WH (2014) Cortical effects of deep brain stimulation: implications for pathogenesis and treatment of Parkinson disease. JAMA Neurol 71:100–103.

Li S, Arbuthnott GW, Jutras MJ, Goldberg JA, Jaeger D (2007) Resonant antidromic cortical circuit activation as a consequence of high-frequency subthalamic deep-brain stimulation. J Neurophysiol 98:3525–3537.

Limousin P, Pollak P, Benazzouz A, Hoffmann D, Le Bas JF, Perret JE, Benabid AL, Broussolle E (1995) Effect on parkinsonian signs and symptoms of bilateral subthalamic nucleus stimulation. Lancet 345:91–95.

Lozano AM, Lipsman N, Bergman H, Brown P, Chabardes S, Chang JW, Matthews K, McIntyre CC, Schlaepfer TE, Schulder M, Temel Y, Volkmann J, Krauss JK (2019) Deep brain stimulation: current challenges and future directions. Nat Rev Neurol 15:148–160.

McCarthy M, Moore-Kochlacs C, Gu X, Boyden E, Han X, Kopell N (2011) Striatal origin of the pathologic beta oscillations in Parkinson's disease. Proc Natl Acad Sci USA 108:11620–11625.

McConnell GC, So RQ, Hilliard JD, Lopomo P, Grill WM (2012) Effective deep brain stimulation suppresses low-frequency network oscillations in the basal ganglia by regularizing neural firing patterns. J Neurosci 32:15657–15668.

McConnell GC, So RQ, Grill WM (2016) Failure to suppress low-frequency neuronal oscillatory activity underlies the reduced effectiveness of random patterns of deep brain stimulation. J Neurophysiol 115:2791–2802.

Miocinovic S, Hemptinne CD, Chen W, Isbaine F, Willie JT, Ostrem JL, Starr PA (2018) Cortical potentials evoked by subthalamic stimulation demonstrate a short latency hyperdirect pathway in humans. J Neurosci 38:9129– 9141.

Mitra P (2007) Observed brain dynamics. Oxford: Oxford UP.

Moro E, Esselink RJ, Xie J, Hommel M, Benabid AL, Pollak P (2002) The impact on Parkinson's disease of electrical parameter settings in STN stimulation. Neurology 59:706–713.

Mulloney B, Selverston A (1972) Antidromic action potentials fail to demonstrate known interactions between neurons. Science 177:69–72.

Pavlides A, Hogan SJ, Bogacz R (2012) Improved conditions for the generation of beta oscillations in the subthalamic nucleus–globus pallidus network. Eur J Neurosci 36:2229–2239.

Paxinos G, Watson C (2007) The rat brain in stereotaxic coordinates, Ed 6, pp 547–612. San Diego: Academic.

Robinson LR, Nielsen VK (1990) Limits of normal nerve function during high-frequency stimulation. Muscle Nerve 13:279–285.

Rosenbaum R, Zimnik A, Zheng F, Turner RS, Alzheimer C, Doiron B, Rubin JE (2014) Axonal and synaptic failure suppress the transfer of firing rate oscillations, synchrony and information during high frequency deep brain stimulation. Neurobiol Dis 62:86–99.

Sanders TH, Jaeger D (2016) Optogenetic stimulation of cortico-subthalamic projections is sufficient to ameliorate bradykinesia in 6-OHDA-lesioned mice. Neurobiol Dis 95:225–237.

So RQ, McConnell GC, Hilliard JD, Grill WM (2011) Irregular high frequency patterns decrease the effectiveness of deep brain stimulation in a rat model of Parkinson's disease. 5th International IEEE/EMBS Conference on Neural Engineering, April 27-May 1, pp 322–325. Cancun: Mexico. https://doi.org/10.1109/NER.2011.5910552.

So RQ, McConnell GC, August AT, Grill WM (2012) Characterizing effects of subthalamic nucleus deep brain stimulation on methamphetamine-induced circling behavior in hemi-parkinsonian rats. IEEE Trans Neural Syst Rehabil Eng 20:626–635.

Stein E, Bar-Gad I (2013) Beta oscillations in the cortico-basal ganglia loop during parkinsonism. Exp Neurol 245:52–59.

Ungerstedt U, Arbuthnott GW (1970) Quantitative recording of rotational behavior in rats after 6-hydroxy-dopamine lesions of the nigrostriatal dopamine system. Brain Res 24:485–493.

Walker HC, Huang H, Gonzalez CL, Bryant JE, Killen J, Cutter GR, Knowlton RC, Montgomery EB, Guthrie BL, Watts RL (2012) Short latency activation of cortex during clinically effective subthalamic deep brain stimulation for Parkinson's disease. Mov Disord 27:864–873.

Weaver FM, et al., CSP 468 Study Group (2009) Bilateral deep brain stimulation vs best medical therapy for patients with advanced Parkinson disease: a randomized controlled trial. JAMA 301:63–73.

Weiss D, Klotz R, Govindan RB, Scholten M, Naros G, Ramos-Murguialday A, Bunjes F, Meisner C, Plewnia C, Krüger R, Gharabaghi A (2015) Subthalamic stimulation modulates cortical motor network activity and synchronization in Parkinson's disease. Brain 138:679–693.

West TO, Berthouze L, Halliday DM, Litvak V, Sharott A, Magill PJ, Farmer SF (2018) Propagation of beta/gamma rhythms in the cortico-basal ganglia circuits of the parkinsonian rat. J Neurophysiol 119:1608–1628.

Yi G, Grill WM (2018) Frequency-dependent antidromic activation in thalamocortical relay neurons: effects of synaptic inputs. J Neural Eng 15:056001.

Yu C, Cassar IR, Sambangi J, Grill WM (2020) Frequency-specific optogenetic deep brain stimulation of subthalamic nucleus improves parkinsonian motor behaviors. J Neurosci 40:4323–4334.

Zheng F, Lammert K, Nixdorf-Bergweiler BE, Steigerwald F, Volkmann J, Alzheimer C (2011) Axonal failure during high frequency stimulation of rat subthalamic nucleus. J Physiol 589:2781–2793.